Nuclear magnetic resonance imaging in pharmaceutical research

Susanta K. Sarkar

Physical and Structural Chemistry Department, SmithKline Beecham Pharmaceuticals, 709 Swedeland Road, King of Prussia, PA 19406, USA

Nuclear magnetic resonance imaging has important applications in pharmaceutical research since it allows specific tissue and disease characterization in animal models noninvasively with excellent anatomical resolution and therefore provides improved ability to monitor the efficacy of novel drugs. We demonstrate here the utility of NMR imaging in renal studies to monitor the mechanism of drug action and renal function in rats. We also discuss the extension of the resolution of an NMR image to microscopic domain at higher magnetic field strengths and the utility of NMR microimaging in cerebrovascular and tumour metastasis studies in mice.

NUCLEAR magnetic resonance imaging is now clinically used to diagnose disease processes[1,2]. In addition to its now widespread clinical use, NMR imaging also has important applications to pharmaceutical research and development since it provides long term non-invasive monitoring of animals for disease processes and the assessment of pharmacological intervention. Since NMR is sensitive to structure and dynamics at the molecular level, magnetic resonance imaging in combination with NMR spectroscopy has the unique feature that it gives not only anatomical information but also provides biochemical information[3,4]. This review will focus on the utility of NMR imaging in drug discovery research, particularly in the area of renal, cerebrovascular and tumour studies performed by us[5-9].

Background

The principles and techniques of NMR imaging are extensively reviewed in references 10 and 11. We will only briefly discuss the typical pulse sequences and the description of the parameters used in the works described here. Also, since in a number of our studies the images are obtained with microscopic resolution, we will outline the fundamentals and limits of NMR microimaging.

Imaging sequences

Spin echo. The commonly used spin-echo pulse sequence[12] for 2D Fourier imaging is shown in Figure 1. The first step in this sequence is to select a slice in the

xy plane by applying a field gradient (G_z) along the *z* axis and a selective 90° pulse. The amplitude of the field gradient, G_z, and the bandwidth of the selective pulse determine the slice thickness. The time-reversal gradient is applied to remove the unwanted dephasing after the slice selection. Once a slice is selected, spatial information is encoded in the *x*-direction by acquiring an echo in the presence of the read gradient, G_x. Application of phase-encoding gradient, G_y after excitation produces the spatial information in the *y*-direction of the *xy* plane.

The phase-encoding gradient is incremented in small steps and an echo is acquired for each value of G_y. In order to properly refocus the magnetization during echo acquisition the read gradient (G_x) is turned on during the phase-encoding period.

The expression for the signal intensity at any point of the image obtained using the spin-echo sequence is given by[11]

$$S = N_H [1 - 2 \exp(-TR/T_1) \exp(-TE/2T_1)$$
$$+ \exp(-TR/T_1)] \exp(-TE/T_2),$$

where N_H is the number of protons, TR is the repetition time between each scan and TE is the echo time, as shown in Figure 1. The contrast in the images can be weighted to the spin density or the relaxation time T_1 or T_2 by appropriate choice of TE and TR.
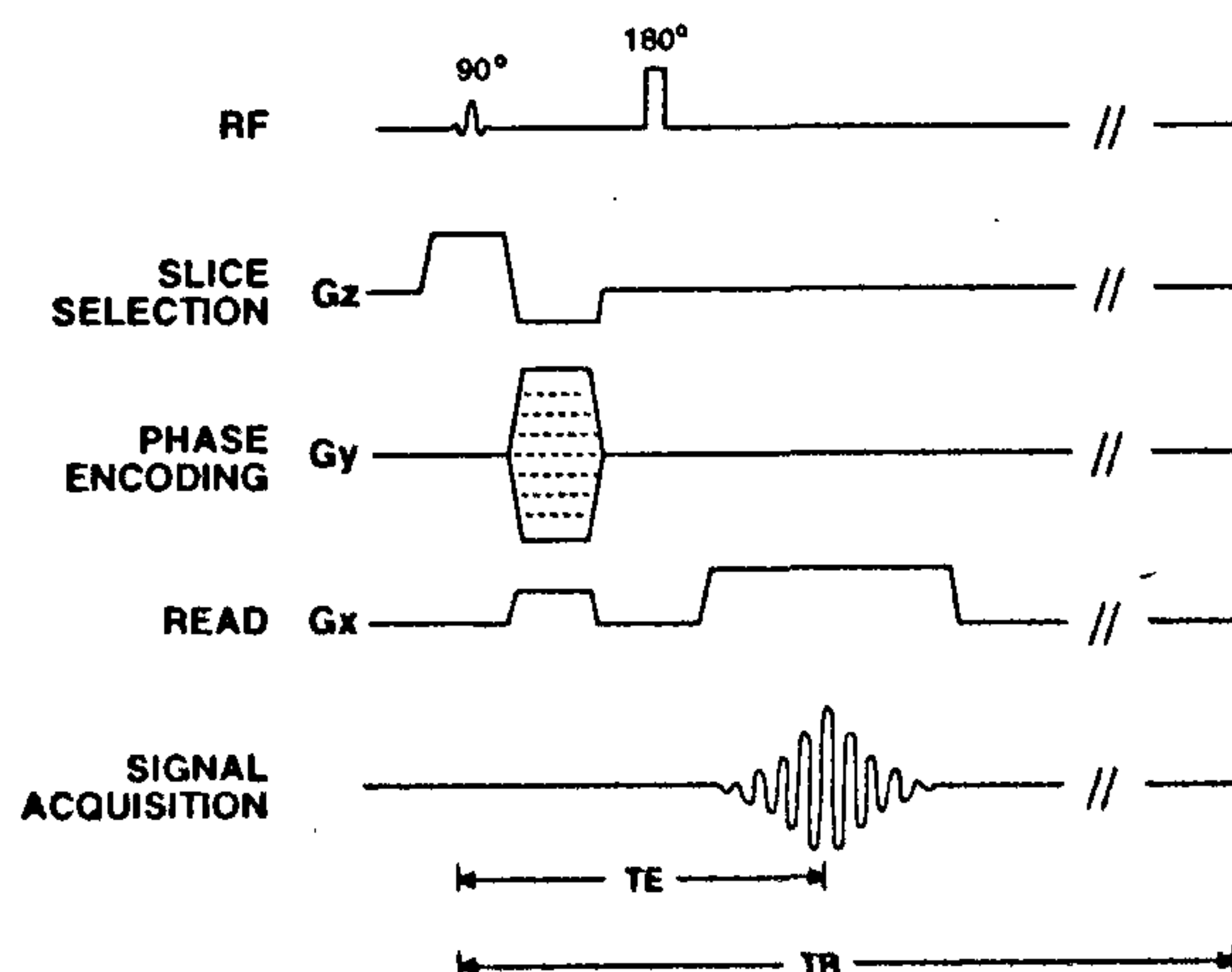

Figure 1. Pulse sequence of spin-echo imaging.

Gradient echo. In the spin-echo sequence, a considerable delay (preferably 3–5 T_1) between each scan is required to account for the relaxation of the longitudinal magnetization. However, this dependence on T_1 or TR could be minimized by reducing the pulse angle from 90° to the Ernst angle, θ, as this maintains the signal-to-noise ratio (SNR) per unit time[13].

$$\theta = \cos^{-1} \exp(-TR/T_1).$$

This is the approach used in the fast-imaging sequences, FLASH (fast low angle shot) or GRASS (gradient recalled acquisition in the steady state)[14], shown in Figure 2, to reduce the imaging time. Here again a slice is selected in the xy plane with application of a field gradient along the z direction and a selective pulse. Under the influence of a negative x gradient (G_x), the transverse magnetization is dephased, while the y gradient simultaneously phase encodes the y dimension. The application of the positive-read gradient (G_x) leads to a rephasing of the magnetization of the observed slice, and eventually to a coherent state and the signal is detected as a 'gradient echo'. Since this method does not necessarily require thermal equilibrium of the magnetization prior to the pulse sequence, images can be obtained within a very short time, from 100 msec to few seconds. However, the lack of the refocusing 180° pulse, necessary for spin echo, makes this sequence more sensitive to the magnetic field inhomogeneities.

In the GRASS sequence the signal strength is given by[11]

$$S = \frac{N_H[(1-\exp(-TR/T_1))\exp(-TE/T_2)\sin\theta]}{[1-\exp(-TR/T_1)\exp(-TR/T_2)-(\exp(-TR/T_1)}$$
$$-\exp(-TR/T_2))\cos\theta].$$

The contrast of images in this sequence is produced by varying the excitation angle θ, TE and TR.
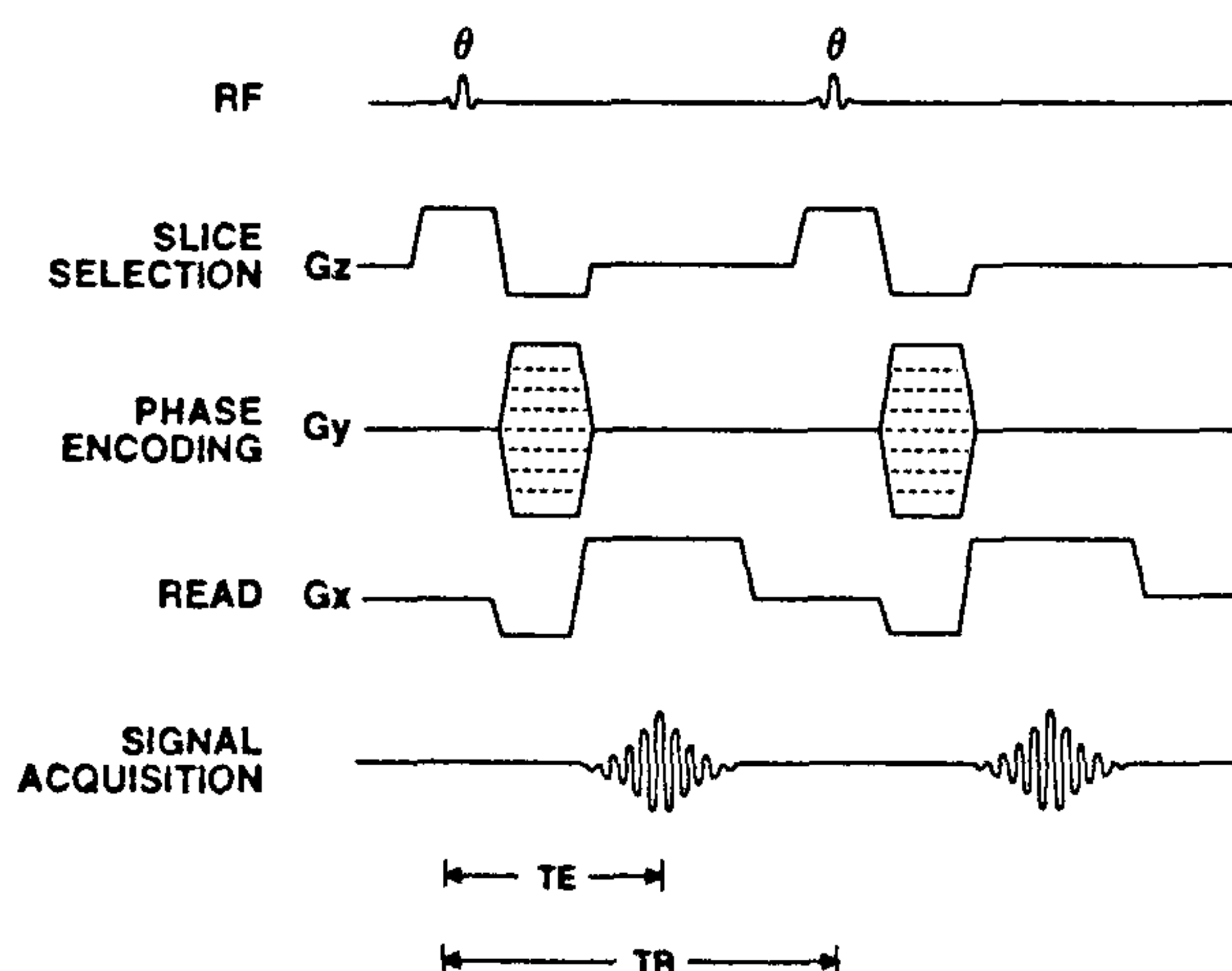

Figure 2. Pulse sequence of GRASS imaging.

Image resolution

In general, clinical images are obtained with mm level resolution. The spatial resolution has been extended to the microscopic domain in NMR microimaging[15,16]. The ability of obtaining images with microscopic resolution has particular advantages for studies of small animals, e.g. rats and mice, animal model used most frequently in pharmaceutical research. However, there are some limitations on the achievable spatial resolution imposed both by the intrinsic and extrinsic factors[17-20].

Intrinsically, spectral linewidth imposes a limit to the spatial resolution (Δx) through spin–spin relaxation time T_2; however this limitation could be minimized by increasing the gradient strength G_x, as is evident from the equation

$$\Delta x = 2/\gamma G_x T_2 \text{ (where the linewidth } \Delta v = 1/\pi T_2),$$

Molecular diffusion may also limit the achievable resolution because of the uncertainty of the position of spins due to Brownian motion during image acquisition.

Among the extrinsic factors, the inhomogeneity or instability of the static magnetic field must be smaller than, or equal to the inhomogeneity induced by the gradients during the experiment for any given resolution in an image; linearity of field gradients is important, as the nonlinearity of gradients induces image distortion and thus degrades the spatial resolution in the nonlinear region of the field; and finally, signal-to-noise ratio (SNR) is the major limiting factor for the achievable resolution in NMR microimaging. The SNR is proportional to the sample volume (V) and the resonance frequency (ω) as follows[21]

$$SNR \propto V \cdot \omega^{7/4},$$

This implies that to improve the spatial resolution of an image from $100 \times 100 \times 100\ \mu m$ to $10 \times 10 \times 10\ \mu m$, the number of accumulations for the same SNR has to be increased by a factor of 10^6 because the SNR deteriorates by a factor of 1000 (assuming the sample volume and the diameter of the transmission and receiving coils remain the same). Since the SNR increases as the (7/4)th power of the magnetic field, we believe that higher magnetic field strengths are necessary for microimaging experiments.

Application of NMR imaging and microimaging

Renal studies

Mechanism of action of drugs. The ability of NMR imaging to distinguish renal cortex and medulla has

recently been demonstrated[5,22,23]. The kidney is the principal organ that regulates water balance in mammals and it has been suggested that renal relaxation times reflect its state of hydration. The renal cortex is made up of predominantly proximal and distal convoluted tubule segments which are responsible for reabsorption of some 70–80% of the glomerular filtrate. The inner medulla consists predominantly of collecting ducts and thin limbs of loops of Henle. Differences in water-handling properties of the two regions may lead to a difference in the relaxation gradients observed between renal cortex and medulla. Thus the effects of diuretic agents which work with different mechanisms could be distinguished by following the changes in the renal cortical–medullary relaxation gradients in the NMR image.

Figure 3 shows the image of a hydropenic rat kidney[24]. Although the image was collected on a whole body 1.5-T instrument, it shows sufficient resolution to define cortex, outer medulla and inner medulla or papilla regions with different intensities. The effect of furosemide (60 mg kg^{-1}), selective for cortical diuresis, and a vasopressin antagonist, [1-(β-mercapto-β,β-cyclopentamethylenepropionic acid), 2-(O-ethyl)D-Tyr, 4-Val,8-Arg,9-desGly] vasopressin (500 μg kg^{-1}), selective for medullary diuresis, on the rat kidney images are shown in Figures 4 and 5 respectively. Furosemide completely dissipates the T_2 gradients (Figure 4), whereas the vasopressin antagonist has practically no effect on the image (Figure 5).

Cortex (C) and papillary (P) signal intensities prior to and following drug administration are expressed as a ratio to that of nearby skeletal muscle and are presented in Figure 6. It is clear from the figure that the C–P T_2 gradient present in hydropenic rats is completely dissipated by furosemide in 15 min, as the cortical T_2 relaxation time increases to the inner medullary level, reflected by an increase in signal intensity. However, the

Figure 3. 1.5-T image of a 48-h-hydropenic rat kidney obtained using spin-echo sequence with a TR of 2.5 sec and TE of 80 msec.

vasopressin antagonist has little effect on T_2 gradients. That furosemide and the vasopressin antagonist acted as diuretics is evidenced by the fact that they both increased the urine flow rate (monitored by swelling of the urinary bladder seen in the NMR images) and diluted urine osmolality (Table 1).

These results demonstrate that renal C–P T_2 gradients represent a physiological function of water handling in rat kidney. Although the precise nature of this function is not known, the phenomenon appears to be related to changes in regional tissue water volume as a function of total volume. Furosemide blocks sodium chloride reabsorption in the thick ascending limb of Henle and results in an enormous increase in delivery of salt (and associated water=filtrate) to the distal tubule[25]. The increase in delivery of filtrate to distal tubules increases the fractional water content at the
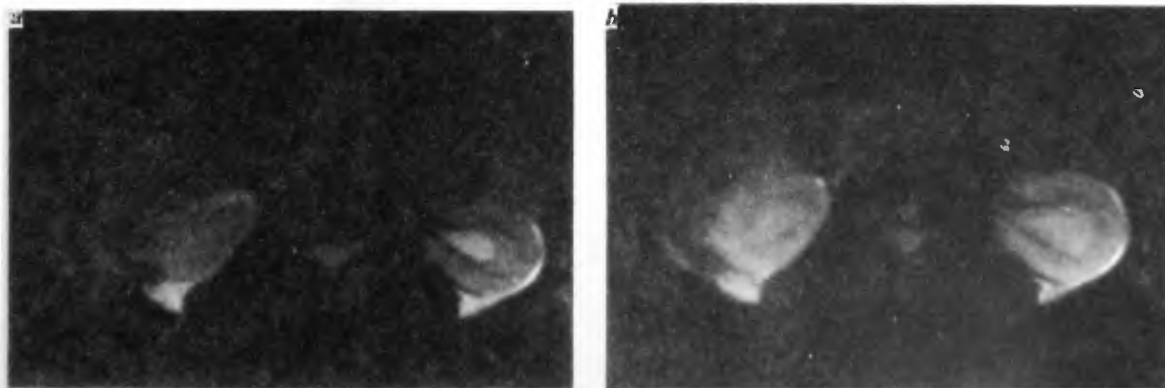

Figure 4. 1.5-T image of a 48-h-hydropenic rat kidney (a) before and (b) 30 min after administration of furosemide obtained using a spin-echo sequence with a TR of 2.5 sec and TE of 80 msec.
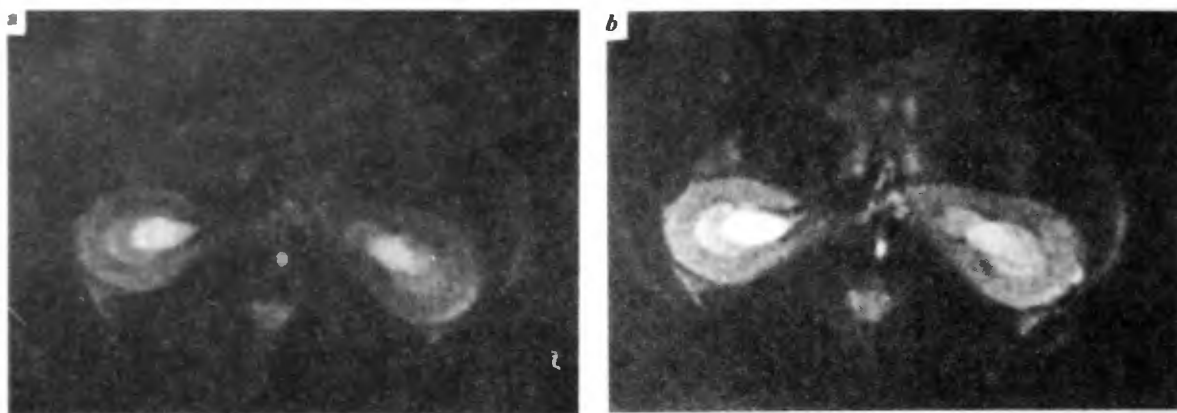
Figure 5. 1.5-T image of a 48-h-hydropenic rat kidney (*a*) before and (*b*) 30 min after administration of the vasopressin antagonist obtained using a spin-echo sequence with a *TR* of 2.5 sec *TE* of 80 msec.
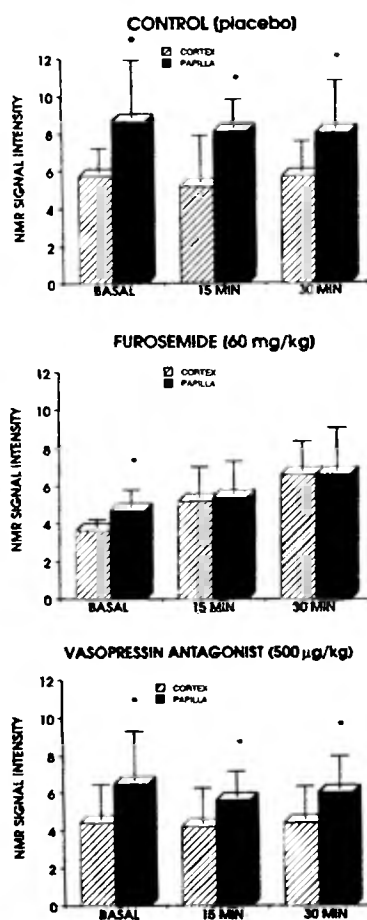

Figure 6. Plot of the changes in renal cortico–papillary intensity gradients in rat kidney following administration of furosemide and the vasopressin antagonist. Intensities are expressed as a ratio of NMR signal intensity of rat cortex and papilla to adjacent muscle (*n* = 3 per group). Values are mean ± SE (* *P* < 0.05).

cortex. Because the excess salt is retained within the tubules (as evidenced by the diuresis), the increase in fractional water content is predominantly luminal water. A closer examination of Figure 4,*a* and 4,*b* reveals an increase in renal size (due to cortical diuretics) during water diuresis, a finding consistent with swelling of the cortex.

The vasopressin antagonist blocks only vasopressin-dependent water reabsorption in the collecting tubules and ducts. The changes in urine osmolality associated with it is accomplished with only a four-fold increase in urine flow rate (or 75% reduction in collecting duct water reabsorption). The increase in medullary flow associated with furosemide was even greater than that associated with the vasopressin antagonist, due to the increase in salt delivery. The lack of the effect of the vasopressin antagonist on renal C–P T_2 gradients is consistent with the fact that this diuretic agent does not substantially affect medullary thick ascending limb function or increase filtrate delivery to the distal tubule.

These results suggest that it would be possible to follow the mechanism of action of various diuretics using NMR imaging.

Renal function. Some inert organometallic complexes, e.g. ^{51}Cr-EDTA (ethylenediaminetetraacetic acid),

Table 1. Urine osmolality in anesthetized rats before and after furosemide or vasopressin antagonist.

Control (48 h hydropenia)	Furosemide ($60 \ mg \ kg^{-1}$)	Vasopressin antagonist ($500 \ \mu g \ kg^{-1}$)
2687 ± 84 (6)	660 ± 25 (3)	700 ± 149 (3)

Values are mean ± SEM, mOsm/kg H_2O. Samples were expressed from the urinary bladder by massage prior to and at the end of each study, and represent average values, not minimum values (*n*).

^{99m}Tc-DTPA (diethylenetriaminepentaacetic acid), and [169]Yb-DTPA, have been used to estimate glomerular filtration rate (GFR) in experimental animals and humans using nuclear imaging[26-28]. Gd-DTPA is now routinely used in clinical diagnosis to alter image contrast by altering relaxation behaviour of water protons in NMR-imaging studies[1]. We wanted to explore this combination of paramagnetism and renal-handling properties of lanthanide chelates of DTPA or EDTA to see if these molecules would be potentially useful probes in NMR-imaging investigations of renal function.

We have recently developed the contrast agent Yb-DTPA with which the contrast generated in the NMR image arises from the differences in susceptibility between the capillaries containing the contrast agent and the surrounding tissue[6]. We have applied this contrast agent for renal-imaging studies and have compared its renal clearance with that of inulin, a standard agent used for measuring glomerular filtration rate.

Figure 7 represents a comparison of simultaneous inulin and Yb-DTPA clearance determinations for individual 20-min clearance periods in five rats. Correlation of inulin and Yb-DTPA clearance values is highly significant ($P < 0.001$). Inulin and Yb-DTPA clearances are parallel over the range of glomerular filtration rates observed, although Yb-DTPA clearance tends to overestimate the inulin clearance by approximately 15%. Therefore, our results suggest that Yb-DTPA is a reasonable inulin-like marker useful for estimation of glomerular filtration rate and tubule water reabsorption in rats.

In order to monitor the time course of the effect of Yb-DTPA on rat kidney images, we have carried out imaging experiments using the GRASS sequence. Figure 8 shows a series of GRASS images of a rat kidney prior to and following administration of Yb-DTPA (0.17 mmol kg^{-1}).
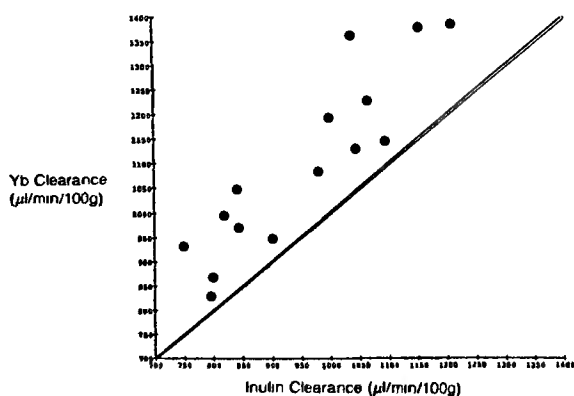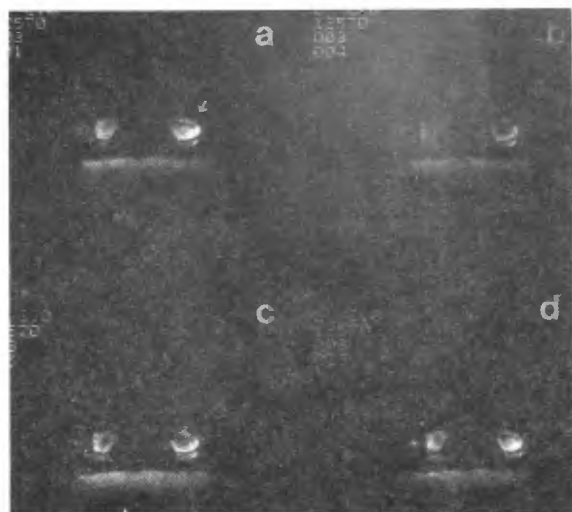

Figure 8. 1.5-T image of a rat left kidney (marked by an arrow) (*a*) before and (*b*) 2 min, (*c*) 9 min, and (*d*) 30 min after administration of Yb-DTPA obtained using a GRASS sequence with a *TR* of 50 msec, *TE* of 22 msec and a flip angle (*θ*) of 20°.

A plot of the ratio of NMR signal intensity of the rat papilla to that of the nearby skeletal muscle prior to and following administration of Yb-DTPA as a function of time is shown in Figure 9. As seen in the figure, signal intensity of the papilla is decreased rapidly over the first five min and then returned to nearly baseline levels within 20 min following the administration of Yb-DTPA. The time course of the effect of Yb-DTPA in the papilla is consistent with that anticipated for a drug whose principal route of clearance is by glomerular filtration. Furthermore, as is shown in Figure 7, Yb-DTPA has a renal clearance similar to that of inulin and thus it is reasonable to conclude that it is handled by the kidney predominantly by filtration. Changes in signal intensity from various regions of the kidney following administration of Yb-DTPA reflect the movement of a bolus of glomerular filtrate through the respective regions. As such, rates of change of signal intensities will depend in large part upon the renal glomerular filtration rate.

These results suggest that Yb-DTPA-enhanced NMR imaging may be a useful tool for monitoring changes in glomerular filtration rate.

Cerebrovascular studies

In recent years, NMR imaging has been used to study experimental models of focal ischaemia to define early hemispheric differences in cerebral tissue perfusion[29], to identify cerebral ischaemic damage[30], and to evaluate associated changes in cerebral tissue pathophysiology

Yb Clearance
(µl/min/100g)

Inulin Clearance (µl/min/100g)

Figure 7. Comparison of renal clearance of inulin and Yb-DTPA.
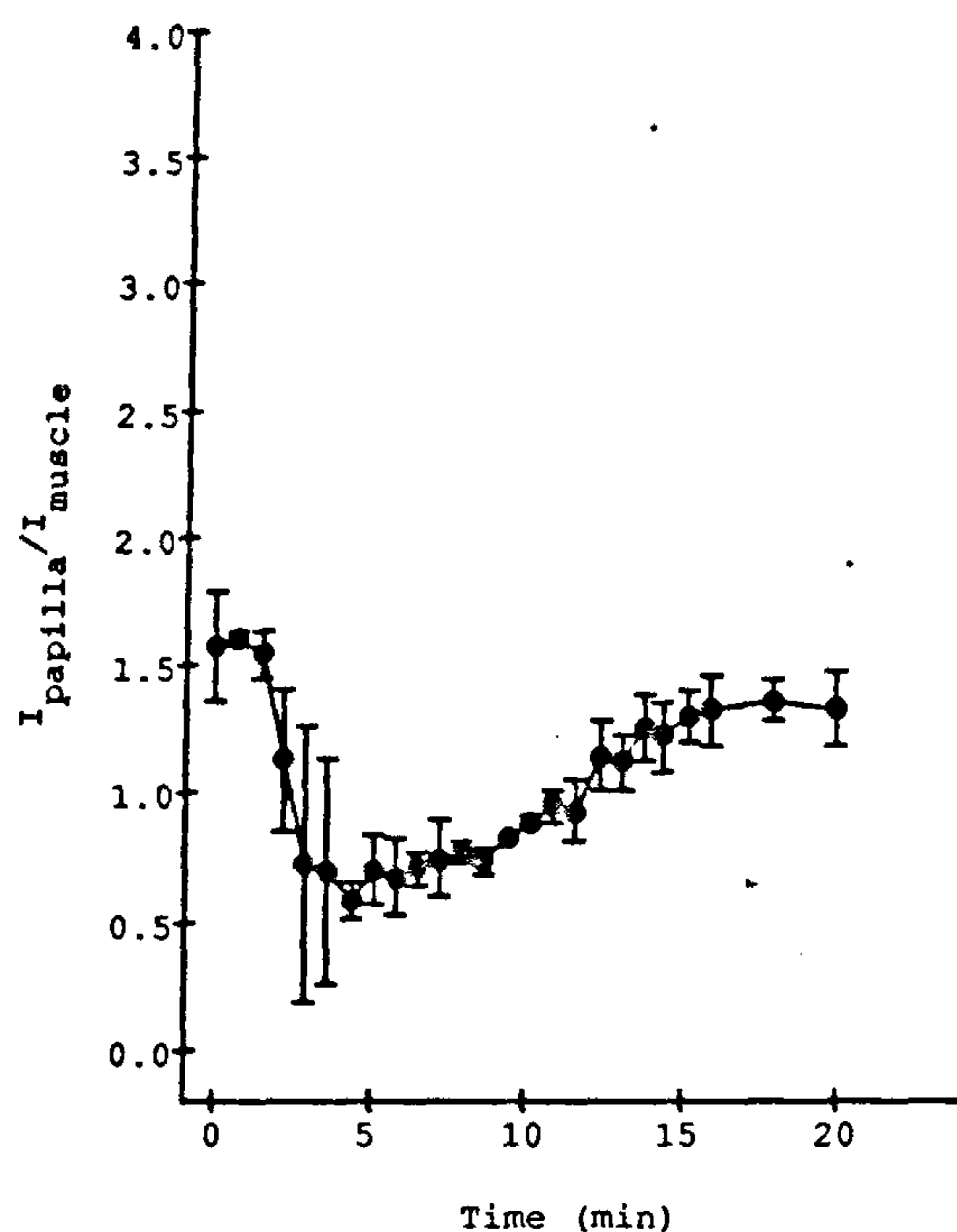
Figure 9. Plot of the ratio of NMR signal intensity of rat papilla to adjacent muscle as a function of time after administration of Yb-DTPA.

and pharmacology[31]. However, a detailed quantitative comparison of the morphological changes identified with NMR imaging and other standard histological techniques is necessary to validate this process.

We have carried out a systematic study to compare, within the same animal, the areas of hemispheric swelling and infarct size following middle cerebral artery occlusion (MCAO) in spontaneously hypertensive rats quantified from NMR imaging with those obtained from gross tissue preparations stained with 2, 3,5-triphenyltetrazolium hydrochloride (TTC) and from histological sections prepared from paraffin-embedded tissue stained with hematoxylin and eosin (H&E)[7].

The left panel of Figure 10 shows a T_2-weighted image of a rat brain two days following MCAO. The image, although obtained with a whole-body instrument operating at 1.5 T, shows sufficient resolution to define the gross morphology and individual hemispheres to match the levels of NMR images with processed tissue sections for comparison. The infarcted regions are shown with a high signal intensity and the contrast between the normal and infarcted zones is obvious, permitting quantitative measurements of infarcted areas in the brain using planimetry. The centre and right panels of Figure 10 show the corresponding two slices

of the same brain stained with TTC and H&E respectively.

The morphological changes seen in the NMR image parallel those observed in stained sections. We have measured the hemispheric swelling and infarct size for each MCAO and sham-operated rat from MRI and compared them to those measured from TTC- and H&E-stained sections. The results are shown in Tables 2 and 3. It is clear from these results that hemispheric swelling and the area of infarction, two parameters of cerebral focal ischaemic damage, can be quantified similarly by NMR imaging and the well-established TTC and H&E histological techniques. Although tissue section thickness differed for the different methods, it was possible to accurately match sections anatomically and make the direct comparison between NMR imaging and histological techniques. Since NMR detection of the ischaemic damage appears to be related to ischaemic or necrotic cell damage and the associated ischaemic tissue oedema, it will be important to utilize quantitative NMR imaging to monitor the dramatic time-related changes in cerebral tissue following focal ischaemia that have been recently identified using histological techniques and their response to drug therapy.

In order to evaluate the efficacy of novel drugs more efficiently, we have now extended our studies of focal ischaemia to mice using microimaging techniques. Figure 11 shows a NMR microimage of a transverse section through a mouse brain with focal ischaemic damage produced by MCAO, collected at 4.7 T using a microimaging probe.

The images were collected with 1-mm slice thickness and the in-plane resolution is $156\,\mu m \times 156\,\mu m$. The image exhibits excellent contrast and the different anatomical regions of the mouse brain are clearly visible. The infarcted region is clearly identified in the image. The extent of hemispheric infarction ranges from 20 to 30% and the NMR microimaging results parallel to those obtained from histological analyses.

We have now extended the NMR microimaging studies of mice to the field strength of 9.4 T. Figure 12 shows a transverse section (700-μm thick) through a normal mouse brain at 9.4 T. The excellent contrast and resolution ($100\,\mu m \times 100\,\mu m$) obtained in this image allow visualization of anatomical details of the mouse brain.

Tumour studies

There are reports from *in vitro* experiments that relaxation times of water in normal and cancerous tissues are different[32]. The measured relaxation times are dependent on the type of cancer, type of tissue involved and on the field strength at which experiments
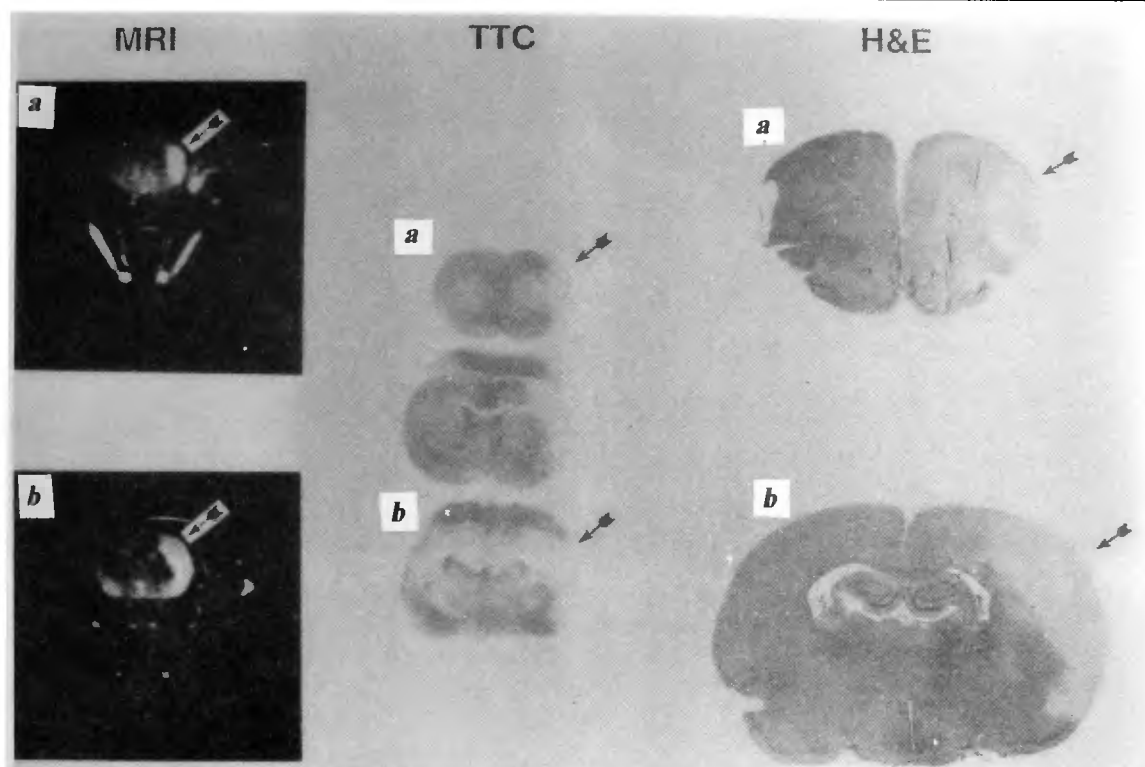
336

Figure 10. Left: 1.5-T image of a rat brain from the level of striatum (*a*) and anterior hippocampus (*b*) obtained using a spin-echo sequence with a *TR* of 2.5 sec and *TE* of 80 msec. The infarcted areas are indicated by arrows. Centre: The corresponding slices of the same brain stained with TTC. The infarcted areas are indicated by arrows. Right: The corresponding slices of the same brain stained with H&E. The infarcted areas are indicated by arrows.

are performed. Although the reason for the difference in relaxation times between the normal and cancerous tissue is not understood, the utility of NMR imaging for the detection and management of cancer has been evaluated. Since we are interested in tumour metastasis and development of anticancer drugs, we wanted to evaluate the potential of high field microimaging in distinguishing normal and neoplastic tissues. Furthermore, NMR microimaging is potentially useful to monitor growth and spread of malignant tumours in metastatic tumour models.

Since the contrast in an NMR image depends on the relaxation times and there were no data available at

Table 2. Per cent hemispheric swelling.

Section level	MCAO (n=6)		
	MRI	TTC	H&E
Striatum	7.1 ± 1.3	8 6 ± 2.1	9.8 ± 3.3
Anterior hippocampus	8 3 ± 1.5	9.4 ± 2.9	7.6 ± 2.0

Table 3. Per cent hemispheric infarct.

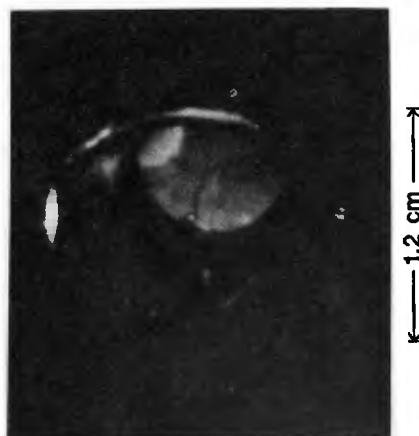| Section level	MCAO (n=6)		
	MRI	TTC	H&E
Striatum	38.1 ± 3.1	33.5 ± 2.7	32.9 ± 2.5
Anterior hippocampus	29.9 ± 4.7	34.6 ± 2.6	33 0 ± 4.0

Figure 11. 4.7-T microimage of a mouse brain with infarction produced by MCAO, obtained using a spin-echo sequence with a *TR* of 3 sec and *TE* of 40 msec. The infarcted area is indicated by an arrow.

Figure 12. 9.4-T microimage of a mouse brain obtained using a spin-echo sequence with a *TR* of 3 sec and a *TE* of 32 msec. A slice thickness of 700 μm was used with in-plane resolution of 100 μm × 100 μm.
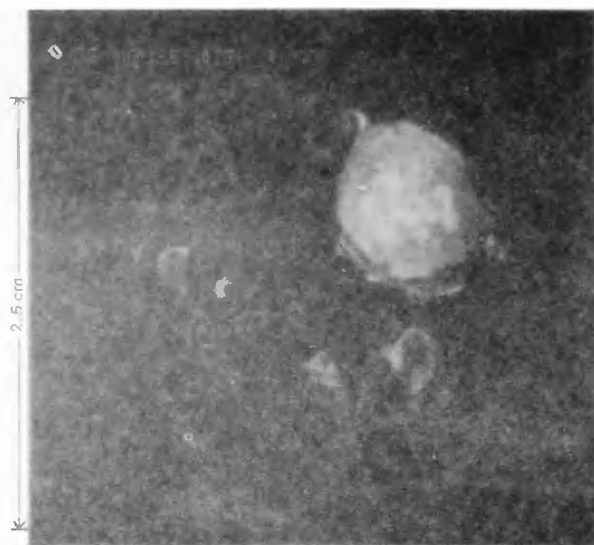

Figure 13. 9.4-T image of a human colon carcinoma xenograft in nude mice obtained using a spin-echo sequence with a *TR* of 3 sec and a *TE* of 32 msec. A slice thickness of 650 μm was used with in-plane resolution of 100 μm × 100 μm.

9.4 T, we measured T_1 and T_2 values of the normal liver and colon adenocarcinoma (HT29) xenografts excised from nude mice and the values are listed in Table 4 (ref. 9). It is clear from the table that the T_2 values of colon carcinoma are significantly longer than those of the normal liver tissue at 9.4 T. We have carried out 9.4 T microimaging studies to follow the progressive growth of human colon adenocarcinoma xenografts in a nude mouse[8].

Figure 13 shows a microimage of a transverse section (650 μm) through human colon carcinoma xenografts in a nude mouse four weeks after the inoculum. The image quality is excellent and the tumour is clearly distinguished from the non-neoplastic tissue. The resolution in the image is 100 μm × 100 μm and at this level considerable heterogeneity is observed, probably because of necrosis[8].

The resolution and contrast observed in this study demonstrate, for the first time, that human tumour xenografts in nude mice can be detected at 9.4 T. Because smaller tumours are detectable with microscopic resolution, we extended the microimaging technique to investigate metastatic-tumour models[9]. To

this end we chose an animal model of the metastatic hepatic lesion of colon cancer (HT29) that mimics several aspects of the human disease[33]. We have also compared the NMR images with the corresponding histological sections[9].

Figure 14 shows an image of a transverse slice (900 μm) through the liver of a nude mouse. The liver lobes and the gall bladder are clearly identifiable in the image, as indicated by the paraffin-embedded tissue of the corresponding sections (Figure 14,*b* and *c*). The tumour deposit (marked by an arrow) is easily distinguishable from normal liver. As shown in the figure, the contrast between the tumour and the liver is excellent and the resolution in the image is 100 μm × 100 μm. The tumour size estimated from the image is 10 pixels or 1.0 mm and this corresponds well with the measurements (900 μm) of the stained section obtained with a stage micrometer.

It is interesting to note that the hepatic tumour deposit (Figure 14,*a*) shows a central dark region, which corresponds to the lumen of a glandular structure as determined by histopathological examination (Figure 14,*c*). This lumen mostly contains dead cells, resulting in lower proton density and thus appears dark in these images. Lumen size (300 μm) estimated by NMR microimaging and by micrometry was in agreement.

These studies suggest that it would be possible to extend the microimaging techniques to study micro-metastasis and its response to experimental therapeutic agents.

Table 4. T_1 and T_2 values* of liver and human colon carcinoma xenografts excised from nude mice.

Tissue	T_1 (sec)	T_2 (msec)
Liver	1.2 ± 0.06	7.7 ± 0 6
Colon carcinoma	2.0 ± 0.04	30.0 ± 0.3

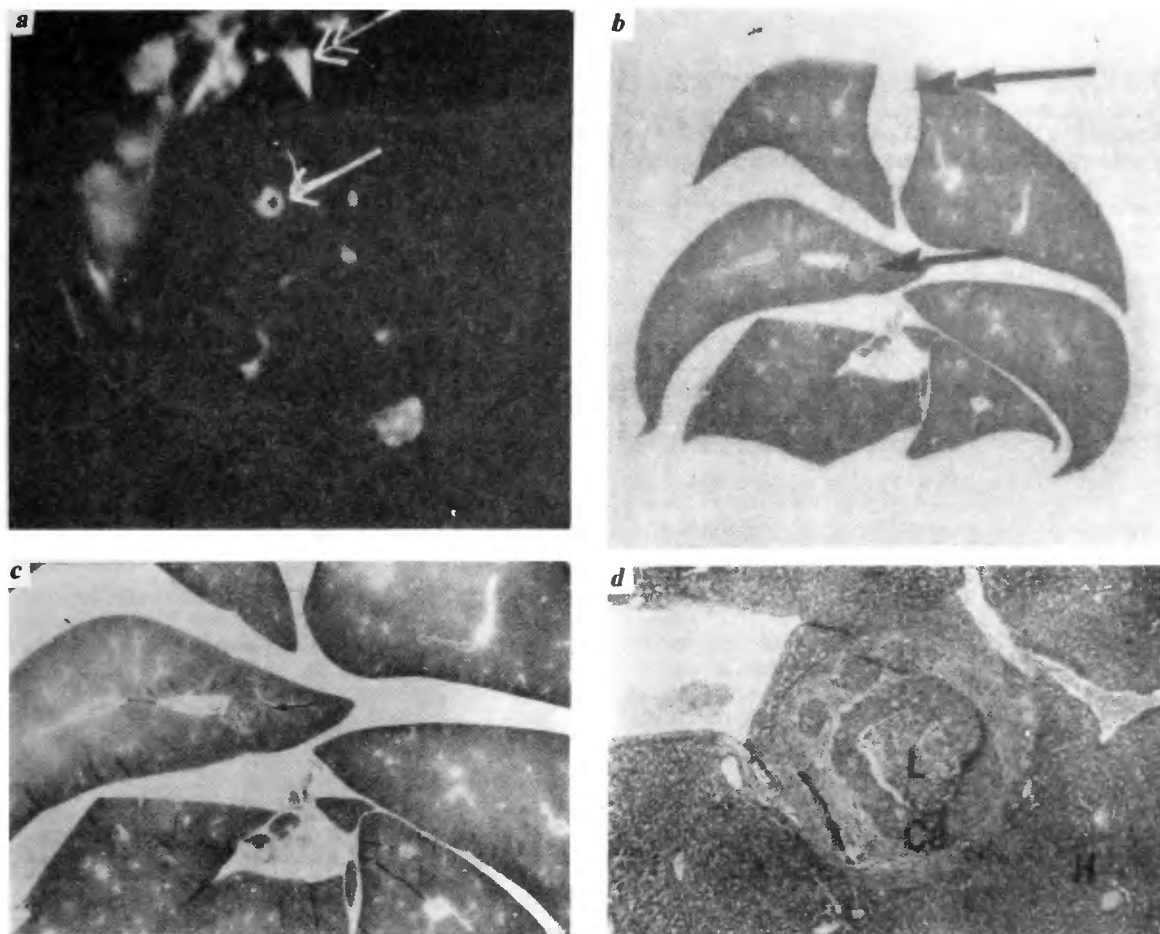*Values are mean ± SD for $n = 3$, measured at 9.4 T.

Figure 14. *a,* 9.4-T microimage of a transverse section through the liver of a nude mouse obtained using a spin-echo sequence with a *TR* of 3 sec and a *TE* of 32 msec. A slice thickness of 900 μm was used with in-plane resolution of 100 μm × 100 μm. The arrow indicates the location of a colon carcinoma hepatic lesion. Note the dark area in the centre of the lesion, corresponding to the gland lumen. The double arrow indicates the location of gall bladder. *b,* Photograph of the parrafin-embedded tissue of the corresponding section. Tumour and gall bladder locations are indicated by the arrow and double arrow respectively. *c,* Same as (*b*) with higher magnification (3.4 ×). *d,* Higher magnification (30 × b) of the lesion shown in (*b*). [Ca, carcinoma; L, gland lumen; H, hepatocytes].

Summary and future potential

In addition to the areas of studies described here, NMR imaging has also been applied in the areas of cardiovascular studies[34,35], arthritis[36], and toxicology and pathology[37,38]. All the images in the studies described here were of protons. Recently, NMR imaging has been extended to other nuclei, e.g. [19]F, [23]Na (refs. 39, 40). [19]F imaging may be useful to study molecular pharmacology of fluorinated drugs *in vivo*. [23]Na imaging monitors, noninvasively, alteration in regional sodium content and thus may provide new insight into the pathophysiology of neoplasia and stroke.

NMR imaging, particularly the microimaging tech-

niques, allows specific tissue and disease characterization in animal models noninvasively with excellent anatomic resolution and therefore provide better understanding of disease pathophysiology and an improved ability to monitor the efficacy of novel drugs. Since in NMR-imaging studies each animal can be used as its own control to monitor the efficacy of drugs, it could significantly reduce the errors due to independent control experiments. Furthermore, it promises reduction in animal usage in preclinical research. Finally, the NMR methods developed in preclinical research may be applicable to clinical trials.

1. Stark, D. D. and Bradley, W. G., *Magnetic Resonance Imaging,* The C. V. Mosby Company, St. Louis, 1988.

2. Steiner, R. E. and Radda, G. K. (eds.), *Nuclear Magnetic Resonance and its Clinical Applications*, Churchill Livingstone, London, 1984.
3. Gupta, R. K. (ed.), *NMR Spectroscopy of Cells and Organisms*, CRC Press, Boca Raton, 1987.
4. Cohen, S. M. (ed.), *Anals of the New York Academy of Sciences*, 'Physiological NMR Spectroscopy: From Isolated Cells to Man', The New York Academy of Sciences, New York, 1987.
5. Sarkar, S. K., Holland, G. A., Lenkinski, R. E., Mattingly, M. and Kinter, L. B., *Magn. Reson. Med.*, 1988, **7**, 117.
6. Sarkar, S. K., Rycyna, R. E., Lenkinski, R. E., Solleveld, H. A. and Kinter, L. B., *Magn. Reson. Med.*, 1991, **17**, 328.
7. Barone, F. C., Clark, R. K., Feuerstein, G., Lenkinski, R. E. and Sarkar, S. K., *Brain Res. Bull.*, 1991, **26**, 285.
8. Sarkar, S. K., Mattingly, M. A., Kline, T. and Greig, R., *Invest. Radiol.*, 1988, **23**, 677.
9. Sarkar, S. K., Clark, R. K., Rycyna, R. E., Mattingly, M. A. and Greig, R., *Magn. Reson. Med.*, 1989, **12**, 268.
10. Morris, P. G., *Nuclear Magnetic Resonance Imaging in Medicine and Biology*, Clarendon Press, Oxford, 1986.
11. Mansfield, P. and Morris, P. G., *NMR Imaging in Biomedicine*, Academic Press, New York, 1982.
12. Edelstein, W. A., Hutchinson, J. M. S. and Johnson, G., *Phys. Med. Biol.*, 1980, **25**, 751.
13. Ernst, R. R. and Anderson, W. A., *Rev. Sci. Instrum.*, 1966, **37**, 93.
14. Haase, A., Frahm, J. and Matthaei, D., *J. Magn. Reson.*, 1986, **67**, 258.
15. Mansfield, P. and Grannel, P. K., *Phys. Rev.*, 1975, **B12**, 3618.
16. Lauterbur, P. C., *IEEE Trans. Nucl. Sci. NS.*, 1984, **31**, 1010.
17. Eccles, C. D. and Callaghan, P. T., *J. Magn. Reson.*, 1986, **68**, 393.
18. Callaghan, P. T. and Eccles, C. D., *J. Magn. Reson.*, 1987, **71**, 426.
19. Callaghan, P. T. and Eccles, C. D., *J. Magn. Reson.*, 1988, **78**, 1.
20. Cho, Z. H., Ahn, C. B. and Juh, S. C., *Med. Phys.*, 1989, **15**, 815.
21. Hoult, D. I. and Richards, R. E., *J. Magn. Reson.*, 1976, **24**, 71.
22. Kundel, H. L., Schlakman, B., Joseph, P. M., Fishman, J. E. and Summer, S. R., *Invest. Radiol.*, 1986, **21**, 12.
23. Wolf, G. L. and Fobben, E. S., *Invest. Radiol.*, 1984, **19**, 324.
24. Kinter, L. B., Shier, W., Flamenbaum, W. and Beeuwkes, R., *Renal Physiol.*, 1982, **5**, 278.
25. Weiner, I. M. and Mudge, G. H., in *The Pharmacological Basis of Therapeutics* (eds. Gilman, A. G., Goodman, L. S., Rall, Murad, T. W.), MacMillan, New York, 1985.
26. James, A. E., Hosain, F., DeLand, F. H., Reba, R. C., Wagner, H. N. and North, W. A., *J. Can. Assoc. Radiol.*, 1971, **22**, 136.
27. Klopper, J. F., Hauser, W., Atkins, H. L., Eckelman, W. C. and Richards, P., *J. Nucl. Med.*, 1972, **13**, 107.
28. Reba, R. C., Hosain, F. and Wagner, H. N., *Radiology*, 1968, **90**, 117.
29. Bradley, R. H., Kent, T. A., Eisenberg, H. M., Quast, M. J. and Ward, G. A., *Stroke*, 1989, **20**, 1032.
30. Brant–Zawadzki, M., Weinstein, P., Bartowski, H. and Moseley, M., *AJR*, 1987, **148**, 579.
31. Sauter, A. and Rudin, M., *Stroke*, 1986, **17**, 1228.
32. Beall, P. T., Amtey, S. and Kasturi, S. R., *NMR Data Handbook for Biomedical Applications*, Pergamon Press, New York, 1984.
33. Clark, R. K., Turner, N. A., Sarkar, S. K. and Greig, R., Abstract of the International Symposium on Critical Determinants in Cancer Progression and Metastasis, Houston, TX, 1989.
34. Sarkar, S. K. and Macartney, L. N., Unpublished results.
35. Caputo, G. R., Sechtem, U., Tscholakoff, D., Higgins, C. B., *AJR*, 1987, **149**, 237.
36. Borah, B. and Szevereny, N. M., *Magn. Reson. Med.*, 1990, **15**, 246.
37. Johnson, G. A. and Maronpot, R. R., *Toxicol. Pathol.*, 1989, **17**, 613.
38. Johnson, G. A., Thompson, M. B., Gewalt, S. L. and Hayes, C. E., *J. Magn. Reson.*, 1986, **68**, 129.
39. McFarland, E., Koutcher, J. A., Rosen, B. R., Teicher, B. and Brady T. J., *J. Comput. Ass. Tomog.*, 1985, **9**, 8.
40. Ra, J. B., Hilal, S. K. and Cho, Z. H., *Magn. Reson. Med.*, 1986, **3**, 296.

Image-guided *in vivo* proton magnetic resonance spectroscopy in human brain

Ponnada A. Narayana and Edward F. Jackson

The University of Texas Health Science Center at Houston, Department of Radiology, 6431 Fannin, MSMB 2.132, Houston, Texas 77030, USA

Image-guided *in vivo* proton magnetic resonance spectroscopy (MRS) studies of human brain are described. The technical requirements for performing these studies are briefly reviewed. *In vivo* proton MRS brain studies of normal volunteers, patients with multiple sclerosis, and ischaemic brain injury are presented.

THE introduction of powerful Fourier-transform (FT) techniques and continuously decreasing costs and expanding power of computers have propelled nuclear magnetic resonance (NMR) into diverse disciplines. In the last two decades NMR has also been added to the armamentation of diagnostic tools employed in clinics. Because of the connotation the word 'nuclear' carries to a lay person, NMR is simply referred to as magnetic resonance or MR by clinicians and scientists involved in human research. Unfortunately, this nomenclature is a misnomer because magnetic resonance includes not only nuclear magnetic resonance but also electron paramagnetic resonance. Nevertheless, to be consistent with the biomedical literature, we use MR instead of NMR in this review.

340